ACS APPLIED MATERIALS & INTERFACES
Research Article
www.acsami.org

Investigation of Embedded Perovskite Nanoparticles for Enhanced Capacitor Permittivities

Andreas Krause,*[†] Walter M. Weber,[†] Darius Pohl,[‡] Bernd Rellinghaus,[‡] Marcel Verheijen,[§] and Thomas Mikolajick[†,∥]

[†]NaMLab gGmbH, Noethnitzer Strasse 64, 01187 Dresden, Germany

[‡] Institute for Metallic Materials, Leibniz Institute for Solid State and Materials Research (IFW) Dresden, P.O. Box 270116, 01171 Dresden, Germany

[§]Department of Applied Physics, Eindhoven University of Technology, P.O. Box 513, 5600 MB Eindhoven, The Netherlands

[∥]Institute of Semiconductors and Microsystems, Dresden University of Technology, 01062 Dresden, Germany

Supporting Information

ABSTRACT: Growth experiments show significant differences in the crystallization of ultrathin $CaTiO_3$ layers on polycrystalline Pt surfaces. While the deposition of ultrathin layers below crystallization temperature inhibits the full layer crystallization, local epitaxial growth of $CaTiO_3$ crystals on top of specific oriented Pt crystals occurs. The result is a formation of crystals embedded in an amorphous matrix. An epitaxial alignment of the cubic $CaTiO_3$ $\langle 111 \rangle$ direction on top of the underlying Pt $\{111\}$ surface has been observed. A reduced forming energy is attributed to an interplay of surface energies at the $\{111\}$ interface of both materials and $CaTiO_3$ nanocrystallites facets. The preferential texturing of $CaTiO_3$ layers on top of Pt has been used in the preparation of ultrathin metal−insulator−metal capacitors with 5−30 nm oxide thickness. The effective $CaTiO_3$ permittivity in the capacitor stack increases to 55 compared to capacitors with amorphous layers and a permittivity of 28. The isolated $CaTiO_3$ crystals exhibit a passivation of the $CaTiO_3$ grain surfaces by the surrounding amorphous matrix, which keeps the capacitor leakage current at ideally low values comparable for those of amorphous thin film capacitors.

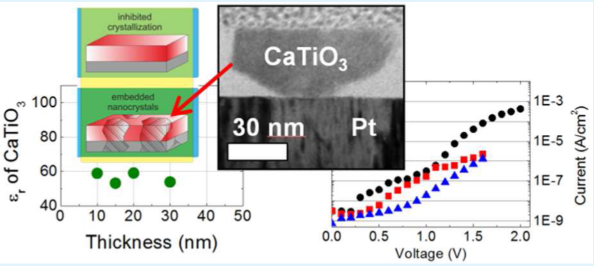

KEYWORDS: *perovskites, nanocrystallites, dielectrics, local epitaxy, surface energy*

1. INTRODUCTION

Perovskites are a well-known group of materials with multifunctional properties such as high permittivity,[1−4] ferro- and piezoelectricity,[5,6] superconductivity,[7−9] and ferromagnetism.[10] With small substitutions of the perovskite crystal structure, the conductivity can be tuned from insulating toward metallic behavior, for example, for colossal magnetoresistance[11] or transparent conductors.[12] All these perovskite materials and their properties have opened access to considerable research activities and multiple applications.

Previous calculations for perovskites done in literature investigate the surface energy of specific surfaces or ferroelectricity at interfaces or grain boundaries by introducing lattice strain. Recent experiments on perovskites accessed the nanoscale region with the growth of nanowires[13,14] and nanoparticles.[15,16] So far, $CaTiO_3$ has not found its way in the preparation of nanostructured devices. Recent results of strain engineering on typically paraelectric $CaTiO_3$ show ferrielectric behavior at the grain boundaries[17,18] or ferroelectricity at surfaces.[19] The possibility to control the number and surrounding of grain boundaries can therefore be used for future device applications.

In this work, we show a detailed study of perovskite nanocrystallites surrounded by an amorphous matrix for the case of sputter deposited $CaTiO_3$. Capacitors with those embedded nanocrystallites exhibit an intermediate permittivity of 50 and above between the permittivity of approximately 105 in a fully crystalline layer and 28 for amorphous $CaTiO_3$ layers.[20] Pt is a suitable material for epitaxial growth of perovskites[21,22] with a lattice constant comparable to $CaTiO_3$.[23] Besides the good lattice match, the selective growth of the nanocrystallites takes advantage of the different surface energies of $CaTiO_3$ and Pt facets. Consequential differences in crystal formation energy result in a preferential growth of crystalline $CaTiO_3$ nanocrystallites in [111] direction on top of the underlying Pt $\langle 111 \rangle$ surface texture. The embedded nanocrystallites further exhibit a surface passivation by the surrounding matrix of amorphous $CaTiO_3$. We show that this effect has been used to significantly reduce leakage currents in 10−30 nm thick metal−insulator−metal (MIM) capacitor stacks. This is an important step to solve the typical trade-off

Received: July 22, 2014
Accepted: October 20, 2014
Published: October 20, 2014

between crystallinity and high permittivity on the one hand and to low leakage current that requires amorphous films on the other hand for dynamic random access memory (DRAM) capacitors.[24,25] This trade-off is nowadays eluded with the use of multilayers,[26] with the disadvantage of low permittivity layers in serial capacitor arrangement.

2. EXPERIMENTAL METHODS

The $CaTiO_3$ layers were sputtered on top of 4 × 4 cm substrates in a 6 in. adapter plate. These substrates consist of an electrically conducting electrode of sputter deposited Pt on top of TiN at 100 °C (p = 1.1 × 10^{-3} mbar, 25 sccm Ar for Pt; p = 1.2 × 10^{-3} mbar, 20 sccm Ar, 4.5 sccm N_2 for TiN) on a highly As-doped (1 × 10^{19} cm^{-3}) Si substrate. For oxide deposition, the substrates are located axis-on-axis approximately 24 cm from the 3 in. target surface to achieve high thickness uniformity. To enable the formation $CaTiO_3$ nanocrystallites in an amorphous matrix, the deposition of the $CaTiO_3$ layers with different thicknesses has been done at varying temperatures between 550 and 600 °C substrate temperature. This is slightly below the temperature of approximately 650 °C for which full crystallization of the whole layer on top of a Si substrate was achieved in previous investigations.[27] The deposition rate of $CaTiO_3$ was approximately 0.17 nm/min.

To allow the electrical characterization of the samples, a complete MIM capacitor stack was created with the deposition and structuring of a top electrode (15 nm layer thickness) consisting of TiN or Ru (p =1.2 × 10^{-3} mbar, 20 sccm Ar for Ru) to account for different work functions. The top electrode is structured with the help a metal hard mask as well as removal of TiN with wet etching (5 min in 10:20:500 mL of NH_3 (25%):H_2O_2 (30%):H_2O at 50 °C) and reactive ion etching with O_2 plasma of Ru under the formation of volatile RuO_4. The top electrode structure consists of 70 circles with different diameter (110 μm−450 μm) per die with 6 dies per sample.

To verify the formation of crystallites in the layer, capacitance voltage measurements on 35 of these MIM capacitors were performed to extract the effective permittivity ε_r. This was done at 100 kHz with 50 mV small signal in a shielded semiautomatic probe station. Only capacitors with a dissipation factor below 0.1 have been used for extraction of the capacitance to ensure the validity of the used parallel capacitance measurement model (Cp-D). The measured permittivity is the result of a mixture of permittivities of amorphous and crystalline $CaTiO_3$. The same setup has been used to measure the leakage current of the other 35 capacitors and allowed a correlation between both permittivity and leakage current. The leakage current measurement was performed with a 5 s delay between each measurement step to virtually eliminate relaxation currents. The positive voltage was applied to the conducting substrate via the probe station chuck. The maximum voltage applied has been set to a voltage of approximately 20% below the breakdown voltage.

Selected samples have been further prepared for high-resolution transmission electron microscopy (TEM) measurements.

3. EXPERIMENTAL RESULTS

The crystallization and therefore the permittivity can be controlled by the thermal budget during deposition as well as the oxide layer thickness. The transition from partially crystalline to fully crystalline layers is governed by a sensitive interplay between both the thermal budget and layer thickness. As shown later in Figure 5, the deposition time plays no significant role in the degree of crystallization. $CaTiO_3$ layers thicker than a critical thickness for a chosen deposition temperature crystallize completely. At lower thicknesses, the crystallization is inhibited. This is comparable to experiments using capacitors with ultrathin ZrO_2 layers on top of polycrystalline TiN and single crystalline Si substrates.[28,29] The effect has been related to an inhibited homogeneous crystallization due to the reduced formation energy according to the work of Zacharias et al.[30] and Wei et al.[31] Nevertheless, the system with a polycrystalline bottom layer with a comparable lattice to the $CaTiO_3$ layer has so far known not been investigated in experiments before.

Figure 1 shows a bright field transmission electron microscopy (BFTEM) cross-sectional image of a $CaTiO_3$ layer deposited at 600 °C on top of polycrystalline Pt. The darker parts indicate $CaTiO_3$ crystallites embedded in an amorphous matrix of $CaTiO_3$ as brighter areas. The $CaTiO_3$ nanocrystallites exhibit an inverse pyramidal shape starting at the Pt bottom electrode. Figure 1 also shows that a significant $PtSi_x$ formation has been prevented by the deposition of a thin 3 nm TiN layer as a conducting diffusion barrier in between Pt and the Si substrate.

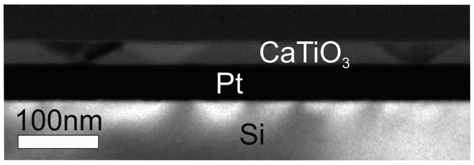

Figure 1. Bright field TEM image of a 30 nm $CaTiO_3$ layer on top of a Pt layer showing various embedded crystallites. The $CaTiO_3$ crystallites show an inverse pyramidal shape starting from the Pt bottom layer.

In Figure 2, a detailed high-resolution TEM (HRTEM) micrograph shows the interface between a single isolated $CaTiO_3$ crystallite and the underlying Pt surface. There is a correlation between the surface orientations of both materials (similar results for another isolated crystallite are shown in Figure S2, Supporting Information). From a specific region of the interface (red rectangle), a fast Fourier transform (FFT) has been taken to allow to extract the crystal orientations and the correlation of both lattices. The FFT pattern displays a [110] zone axis pattern of the Pt crystal with a ⟨111⟩ axis parallel to the Pt surface normal, as expected from a ⟨111⟩ texture of the Pt film. The other strong spots correspond to the $CaTiO_3$ lattice planes visible in the $CaTiO_3$ crystal and can be assigned to {220} and {440}, respectively. The accuracy of the FFT pattern with both Pt and $CaTiO_3$ reciprocal lattice points does not give enough information for the unique assignment of the $CaTiO_3$ zone axis. Nevertheless, with an increased contrast, it was possible to extract the relevant orientations of cubic $CaTiO_3$ (Figure S3, Supporting Information). As a result, both Pt and $CaTiO_3$ crystals are seen in Figure 2 from the [110]

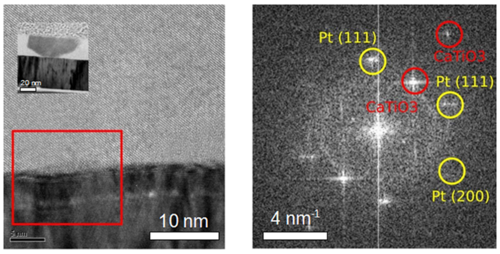

Figure 2. (Left) HRTEM micrograph of the interface between one $CaTiO_3$ nanocrystallite and the underlying Pt surface and (inset) the corresponding embedded nanocrystallite in the 30 nm $CaTiO_3$ layer. The visible dominant lattice planes of $CaTiO_3$ have a distance of 0.27 nm. (Right) The correlation between the lattices of $CaTiO_3$ on top of Pt is presented in the corresponding 2D FFT image.

zone axis. The different intensities of the $CaTiO_3$ reflexes originate from the deformed cubic structure of $CaTiO_3$ crystal where crystal symmetries are broken. The $CaTiO_3$ spots coincide within 90° to the position of the {220} spots of the Pt crystal. Other orientation relations between $CaTiO_3$ crystallites and the Pt layer have not been observed. The low lattice mismatch between Pt ($a = 0.392$ nm)[32] and $CaTiO_3$ ($a = 0.384$ nm)[23,33] suggests a selective-area epitaxial growth of $CaTiO_3$ on top of Pt with 2.0% lattice mismatch.

Figure 3 schematically depicts the lattice in cross-sectional and top views of the $CaTiO_3$/Pt interface, as it correlates to the TEM image of Figure 2. Both the Pt face-centered cubic (fcc) lattice and the $CaTiO_3$ crystal are displayed along the ⟨110⟩ zone axis. The Pt surface is terminated by the {111} lattice plane. The FFT of $CaTiO_3$ shows the (111) lattice planes of the cubic $CaTiO_3$ lattice. The transformation between the orthorhombic and cubic unit cells of $CaTiO_3$ is a simple vehicle to calculate the correct correlation between both lattices (Table S1, Supporting Information). As discussed above, the correct zone axis toward the visible $CaTiO_3$ planes is not clearly extractable from Figure 2 due to the limited reciprocal lattice points. Taking the cubic $CaTiO_3$ unit cell, the view along the (110) zone axis allows an observation of the (111) lattice plane. In this case, the $CaTiO_3$ surface is either terminated by the CaO_3 plane or the Ti plane toward the Pt (111) surface. The oxide termination and the formation of the Pt−O bonding have been calculated previously for the comparable $SrTiO_3$ lattice.[34,35] That supports the CaO_3 termination of the $CaTiO_3$ interface, which has been assumed in Figure 3. Finally, due to the comparably good lattice match of both materials, the depicted simplest correlation of (111) $CaTiO_3$ and (111) Pt is expected and shown in Figure 3b.

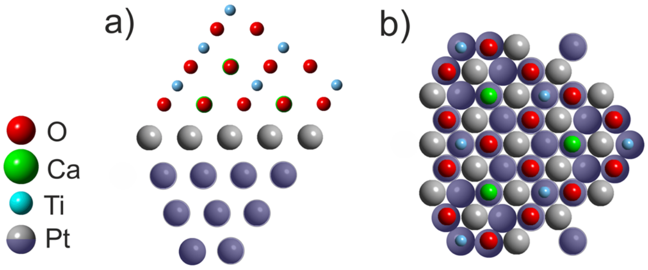

Figure 3. Image of lattice correlation at the interface between the Pt {111} surface and the $CaTiO_3$ crystal. (a) The cross-sectional view of the interface as it has been extracted from the FFT of Figure 2. (b) The extracted top view of both the interfacial atoms of $CaTiO_3$ and Pt shows the stacking of $CaTiO_3$ atoms in relation to the outermost Pt layer (light gray). The suggested correlation is the CaO_3 terminated $CaTiO_3$ surface on top of the underlying Pt {111} interface layer.

The correlation between $CaTiO_3$ and Pt along the ⟨111⟩ direction is a hint toward an epitaxial growth of $CaTiO_3$ crystallites. Interestingly, no orientation relation has been observed other than the one identified in Figure 2 and in Figure S2 (Supporting Information).

4. MECHANISM FOR PARTIAL NUCLEATION

The partial crystallization of $CaTiO_3$ cannot be solely explained by the good epitaxial relationship between Pt and $CaTiO_3$. Due to the comparable (cubic) crystal structure of Pt and $CaTiO_3$, the lattice mismatch of similar directions is identical, and the lattice plane distances d_{hkl} are equal in this case. For all crystal lattice directions, the same epitaxial relationship exists, and $CaTiO_3$ should crystallize completely even on a polycrystalline Pt surface. X-ray diffraction (XRD) measurements indicate, besides the {311} reflex, a {111} texture along the surface normal of the prepared Pt layers (Figure S4, Supporting Information). This could cause the growth of an increased number of $CaTiO_3$ crystallites, as shown in Figure 1, but does not explain why the whole $CaTiO_3$ layer does not crystallize completely. The texture of the Pt grains does not imply the state of each Pt surface facet; the roughness indicates a deviation from the {111} Pt surface facet to other indices. These different surface facets may inhibit the continuous $CaTiO_3$ crystallite growth. The observed partially crystalline $CaTiO_3$ layer suggests that the forming energy of $CaTiO_3$ crystals is different for various Pt facets, with a preferred nucleation on top of the Pt {111} facet. Due to the very low deposition rate of 0.17 nm/min at elevated temperatures, the deposited $CaTiO_3$ is expected to behave in a thermodynamically controlled manner, and the role of kinetic processes to crystallization is negligible. This is supported by the observation that the preferred crystallization is maintained for thicker films that experience a significantly higher thermal budget, as determined by the constant deposition temperature and deposition rate.

According to literature, the nucleation and texture of crystallites are mainly influenced by the underlying substrate and the interface properties. The orientation and growth mode are determined by the involved interface and surface energies. These depend primarily on the strength and nature of the chemical bonds between film and substrate atoms on the one hand and the film atoms on the other hand.[36−38] The observed preferential growth of (111) $CaTiO_3$ crystallites on top of (111) Pt is most likely influenced by the differences in surface energies. Although we do not know the exact contribution of the surface energy to the crystallite formation of $CaTiO_3$, we see the differences as a first approach for explaining the partial growth.

Pt tends to form {111} facets at higher temperature due to the lowest surface energy of the {111} facet.[39−42] The calculated surface properties of $CaTiO_3$ facets[43−47] are briefly summarized in Table S2 (Supporting Information). For all $A^{2+}B^{4+}O_3^{6-}$ perovskites ($CaTiO_3$, $SrTiO_3$, $BaTiO_3$, $PbTiO_3$, $SrZrO_3$, $BaZrO_3$, etc.), the (001) surface exhibits the lowest surface energy.[48]

In growth experiments with $SrTiO_3$ instead of $CaTiO_3$, epitaxial growth of $SrTiO_3$ had been done on top of Pt[21] or vice versa.[34] Nevertheless, differences in growth energy contribution on various surfaces had not been observed for this system. As reported from Asthagiri et al.[35] for the $SrTiO_3$/Pt system, the polar (111) and (110) surfaces form significantly stronger interfaces than the (100) nonpolar surface. Therefore, and according to the simulated surface energies in Table S2 (Supporting Information) for the cubic $CaTiO_3$ surfaces, the {111}-terminated $CaTiO_3$ surface with its largest surface energy is supposed to be the reason for the unique epitaxial formation of a crystalline interfacial $CaTiO_3$ layer. The forming energy of the first $CaTiO_3$ crystalline monolayer is reduced and results in a seeding layer for the epitaxial growth of $CaTiO_3$ at deposition temperatures below the bulk crystallization temperature. The reason for this restricted local reduction is not clear, but we suppose that the large surface energy of $CaTiO_3$ with the formation of the strong bindings between $CaTiO_3$ and Pt along the {111} interface allows a preferred crystallization. Other areas without a "crystalline" monolayer of $CaTiO_3$ stay amorphous in the further layer growth. While a {110} surface of $CaTiO_3$ exhibits just a bit lower surface energy, the reduction of the {110} Pt surface facets at elevated temperatures may prevent any observation of an epitaxial growth of {110} $CaTiO_3$.

For the further crystallite growth, it cannot be concluded that a closed crystalline layer grows in the ⟨111⟩ direction. However, given the nanometer size dimension of the nucleation areas, the line energies at the circumference of the nucleated layer have a strong contribution to the formation energy of the layer. This is a size effect that roughly considers the number of bonds at the interfacial surface. To this end, we propose that small $CaTiO_3$ crystallites nucleate with {110} facets; although, our TEM analysis does not provide the exact facet orientation. The inverse pyramidal structure can be attributed to the {100} passivated surfaces to lower the formation energy of the $CaTiO_3$ crystal. This is similar to the nucleation of Si nanowires described by Schmidt et. al.[49] The crystallite−amorphous interface exhibits a low surface energy formation with {100} CaO or TiO_2 termination. This results in the inverse pyramidal-shaped nanocrystallites, as shown in Figure 1. This is a deviation to the heterogeneous nucleation with the formation of free-standing pyramidal and dome-like crystals observed for PZT and other materials due to island growth.[50−52] The conclusion is that the {111} surface of $CaTiO_3$ with its largest surface energy is preferred for the epitaxial growth along the {111} $CaTiO_3$/Pt interface. As all grown embedded crystallites exhibit the same orientation, the full layer will show epitaxial-like behavior.

When going to higher deposition temperatures or thicker samples with a full crystallized $CaTiO_3$ layer and homogeneous nucleation, the preferential growth on the {111} surface cannot be distinguished in the entire crystallized $CaTiO_3$ layer.

5. EMBEDDED NANOCRYSTALLITES IN AN ULTRATHIN CAPACITOR STACK

5.1. Electrical Characterization. The embedded nanocrystallites of $CaTiO_3$ have been prepared in a thickness series of $CaTiO_3$ in a MIM capacitor stack. $CaTiO_3$ was deposited at a temperature of 550 °C on top of the polycrystalline Pt electrode. The Ru top electrode was deposited afterward at 100 °C and structured with the help of reactive ion etching. Except for the different deposition time of $CaTiO_3$, all other deposition conditions have been kept constant. Figure 4 shows a single isolated crystallite in a complete ultrathin MIM capacitor arrangement, deposited at 550 °C. The comparatively elevated deposition temperatures result in the formation of crystallites, even for the thinnest layers. The preferential epitaxial growth is not limited by the oxide thickness.

Figure 5 shows the permittivity evolution for the different thicknesses. The permittivity values have been extracted from a linear fit of the inverse capacitance over thickness by neglecting any interfacial capacitance. As shown in Figure 5, the permittivity of $CaTiO_3$ increases to a value of at least 55 between 10 and 30 nm thickness instead of 28 for an amorphous $CaTiO_3$ capacitor stack.[20] As depicted in Figure 5, the constant permittivity indicates a linear increase of crystallization with layer thickness. Therefore, this intermediate permittivity is not caused by an interfacial effect. Furthermore, the amount of crystallites does not change. For thicker samples, the measured permittivity increases to 105, and with this increase, the layer fully crystallizes. The inset of Figure 5 shows a typical capacitance voltage measurement of the 20 nm $CaTiO_3$ capacitor. The data follows a positive quadratic curvature with voltage, which is similar to measurements for amorphous $CaTiO_3$ capacitors. The dissipation factor D is below 0.01 in the measured voltage range, which proves the validity of the used Cp-D capacitance model.

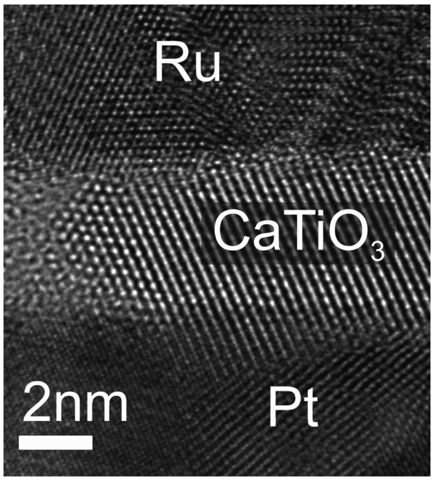

Figure 4. HRTEM image of an embedded crystallite in a MIM capacitor stack with 5 nm oxide thickness. An oxide thickness series revealed an effective permittivity of approximately 55. The crystallization is not limited by the oxide thickness.

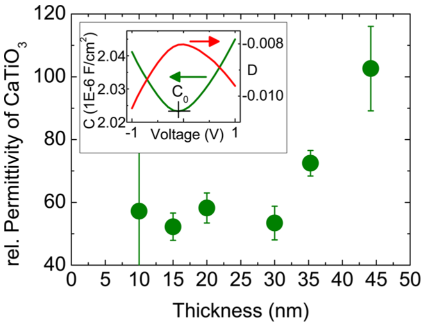

Figure 5. Permittivity of thickness series of $CaTiO_3$ capacitors deposited at 550 °C. For oxide layer thicknesses up to 30 nm, a permittivity of approximately 55 can be extracted due to a partially crystallized $CaTiO_3$ layer. For thicker layers above 30 nm, the permittivity and therefore the crystallinity of $CaTiO_3$ increase up to fully crystalline layers. (Inset) Capacitance voltage measurement of the capacitor with 20 nm $CaTiO_3$. A quadratic dependence of capacitance with voltage is visible.

In Figure 6, the corresponding leakage currents for $CaTiO_3$ layers with different layer thicknesses are plotted. Low leakage currents comparable to amorphous $CaTiO_3$ are shown for the samples between 15 nm (2×10^{-7} A/cm^2 at 1 V) and 30 nm (3.57×10^{-8} A/cm^2 at 1 V) layer thickness. These are extremely low values despite the presence of crystallites (even for stringent applications in DRAM capacitors). High leakage currents are measured, besides the 10 nm sample, for samples with a layer thickness above 30 nm even for low voltages, when crystallinity and permittivity increases. Trap assisted tunneling along numerous defect states at grain boundaries is suggested to be the major leakage mechanism. The strong increase in leakage current for the 10 nm sample can be attributed to the comparatively rough surface of the bottom electrode, as local field enhancement is stronger for thinner dielectrics.

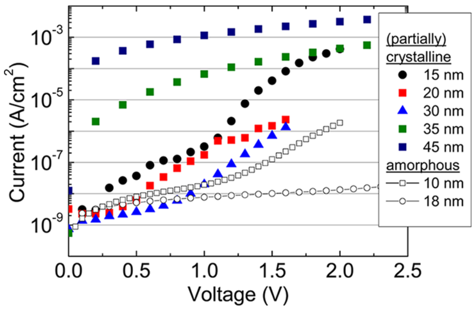

Figure 6. Leakage current as a function of voltage for a thickness series of partially crystalline $CaTiO_3$ with Pt bottom electrode and Ru top electrode. Layers with partially crystalline $CaTiO_3$ exhibit leakage currents comparable to those of amorphous layers.

5.2. Explanation of Reduced Leakage Current. The increase of crystallinity correlates well with the increase in leakage current for the thicker samples. In 10−30 nm thick layers, the permittivity of 55 is the result of a small number of crystallites with high permittivity embedded in the amorphous $CaTiO_3$ matrix with a smaller permittivity of 28. For different layer thicknesses, the constant permittivity of 55 implies a linear increase of crystallinity with increasing the oxide thickness to 30 nm. Distinct to fully crystalline layers, the leakage currents are comparable to those of amorphous samples. The degree of crystallinity is sketched in Figure 7, where the layer develops from isolated $CaTiO_3$ crystals (Figure 7b) to a fully crystallized $CaTiO_3$ stack (Figure 7a). This result strongly suggests that the grain boundaries as main leakage paths[53,54] of the isolated crystallites are passivated by the amorphous matrix. This is in agreement with the observations of Heitmann et al.[55] in a material system of Si/SiO_2. When full layer crystallinity is present, significantly higher conductivity along grain boundaries (yellow sketched dotted paths in Figure 7b) occurs. As a result, with oxide thicknesses greater than 30 nm within the used deposition conditions, crystallinity, permittivity, and leakage current increase significantly.

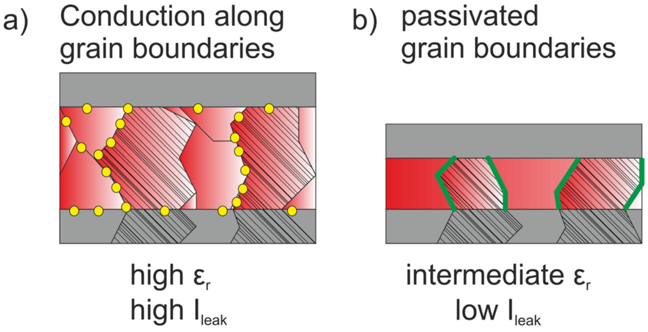

Figure 7. Influence of ordered growth of $CaTiO_3$ in MIM capacitor stack. (a) The ordered growth does not change the conduction behavior for thick and fully crystalline layers. (b) For thin layers, the selective growth result in nanocrystallites embedded in an amorphous matrix. The grain boundaries are passivated (green) with a significant reduction of leakage current compared to fully crystalline layers.

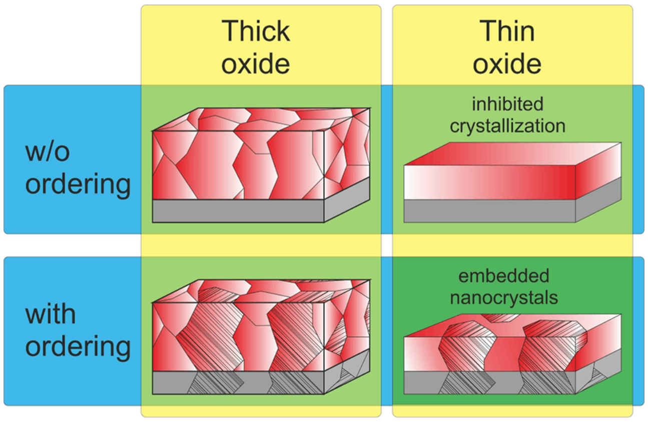

Figure 8. Influence of ordered growth of $CaTiO_3$ on top of Pt compared to samples with unordered growth. Without ordering, the $CaTiO_3$ layer crystallization in thin layers is inhibited. Seeding crystals available from the substrate layer allow ordered growth of $CaTiO_3$ on top of some Pt facets.

6. DISCUSSION

Figure 8 summarizes the influence of the ordering substrate to the degree of structural order in the oxide. For thick layers of $CaTiO_3$, the partially epitaxial growth does not result in a significant change of structural order, the layers are completely crystallized (top left and bottom left images). For thin layers, typically the crystallization is inhibited (top right image).[56] The amorphous-to-polycrystalline phase transition can be described by classical nucleation theory according to Spinella et al.[57] With the help of lattice matched substrate layers working as seeding crystals, the inhibition can be obviated. The polycrystalline Pt surface works as a seeding layer to reduce the forming energy of $CaTiO_3$ crystallites.

From simulations in literature, the {111} $CaTiO_3$ surface exhibits the largest surface energy. We believe this and the CaO_3^{4-} terminated surface with the vacant oxygen atoms are responsible for the preferential growth on only the {111} terminated Pt surface. Obviously, the comparable lattice between Pt and $CaTiO_3$ should not result in any preferential growth on a specific Pt surface. As a result, the $CaTiO_3$ nanocrystallites specifically grow on {111} terminated Pt facets and are simultaneously passivated by the surrounding amorphous matrix (Figure 8, bottom right image).

According to Figure 8, the results were only measurable for ultrathin layers with inhibited layer crystallization. Further analysis is necessary to identify the reason for the preferential growth of $CaTiO_3$ only on the Pt {111} facets. In this study, we used the heterogeneous nucleation to grow embedded nanocrystallites of $CaTiO_3$ in a MIM capacitor stack. The nanocrystallites are passivated by the surrounding amorphous matrix, and as a final result, a reduction of leakage currents with an increased permittivity follows.

The presented results of $CaTiO_3$ as a model system for perovskites may allow preparing isolated crystallites with other materials of the perovskite group. These experiments can focus on the investigation of the amorphous−crystalline interface. We propose to investigate the influence of isolated and ordered crystallites of ferroelectric perovskites with commonly used sputtering techniques. For magnetic perovskites, the passivation may allow the investigation of switching behavior of isolated magnetic domains. Both systems will fill the gap between experiments on polycrystalline layers and isolated (ferroelectric or ferromagnetic) nanoparticles. All our embedded nanocrystallites exhibit the same crystal orientation; therefore, this layer growth results in an epitaxial-like behavior with industry standard sputter deposition technique.

The control and modification of the {111} Pt single crystal surface by, for example, ion beam bombardment can further allow the structured growth of 3D structures already passivated by an amorphous matrix. Thermal treatment of the Pt surface can be used to shift the favorable {111} surface facets to higher proportions.

7. CONCLUSION

The results presented in this work allow the search and investigation of samples with nanocrystallites surrounded by an amorphous matrix. Selected samples have been investigated with TEM to gain knowledge of the crystallinity for maximum permittivity of $CaTiO_3$ in thin films. The reason for intermediate values of permittivity has been correlated to partially crystallized $CaTiO_3$ layers. The formation of crystallites is substantially influenced by the Pt bottom electrode. There is a preferential growth of {111} $CaTiO_3$ crystals on top of a Pt {111} surface resulting in isolated crystals in an otherwise amorphous matrix. This preferential growth does not benefit from good epitaxial relations of various crystal directions but from differences in surface energy of $CaTiO_3$ contributing to the interface energy of the $CaTiO_3$/Pt interface. Going to higher deposition/annealing temperatures and layer thicknesses, the layers become fully crystallized, and the preferentially oriented crystallites are overshadowed by the formation of unordered crystallites. The prepared layers exhibit an intermediate permittivity of 55 with low leakage currents comparable to currents in amorphous layers. This obviates the typical trade-off in application between full crystallinity and high permittivity on one hand and low leakage currents on the other hand for DRAM capacitor applications, for example.

■ ASSOCIATED CONTENT

Ⓢ Supporting Information

The transformation from a (pseudo-) cubic lattice toward the complex orthorhombic lattice with tilted TiO_6 octahedrons of $CaTiO_3$; the correlation between the lattice planes of the cubic and orthorhombic crystals; literature overview of simulated surface energies of cleaved and relaxed cubic $CaTiO_3$ for various surface terminations and different methods; another HRTEM micrograph of a different crystallite for the extracted growth orientation of (111) $CaTiO_3$ on top of (111) Pt; $CaTiO_3$ FFT; and an XRD measurement in Bragg−Brentano geometry of the sample presented in Figure 1. This material is available free of charge via the Internet at http://pubs.acs.org.

■ AUTHOR INFORMATION

Corresponding Author

*E-mail: Andreas.Krause@namlab.com.

Author Contributions

The manuscript was written through contributions of all authors. All authors have given approval to the final version of the manuscript.

Funding

The work was partially supported within the scope of technology development by the EFRE fund of the European Community and by funding of the Free State of Saxony (Project 12462/2043).

Notes

The authors declare no competing financial interest.

■ ACKNOWLEDGMENTS

The authors want to thank the colleagues of Namlab for their support and Tina Sturm from the Leibniz Institute for Solid State and Materials Research Dresden (IFW Dresden) for several TEM sample preparations. Special thanks goes to Uwe Gaitzsch (IFW Dresden) to verify the Pt texture measurements. Also, Wytze Keuning (Eindhoven University of Technology) is acknowledged for TEM sample preparation using focused ion beam (FIB). The authors further want to thank R. Eglitis, H. S. Leipner and J. Heitmann for fruitful discussions and J. Dshemuchadse (ETH Zürich) for the crystal building.

■ REFERENCES

(1) Barrett, J. H. Dielectric Constant in Perovskite Type Crystals. *Phys. Rev.* **1952**, *86*, 118.

(2) Waser, R. Dielectric Analysis of Integrated Ceramic Thin Film Capacitors. *Integr. Ferroelectr.* **1997**, *15*, 39−51.

(3) Ono, K.; Horikawa, T.; Shibano, T.; Mikami, N.; Kuroiwa, T.; Kawahara, T.; Matsuno, S.; Uchikawa, F.; Satoh, S.; Abe, H. (Ba,Sr)TiO_3 Capacitor Technology for Gbit-Scale DRAMs. *Tech. Dig. - Int. Electron Devices Meet.* **1998**, 803−806.

(4) Wallace, R. M.; Wilk, G. D. High-K Dielectric Materials for Microelectronics. *Crit. Rev. Solid State Mater. Sci.* **2003**, *28*, 231−285.

(5) Damjanovic, D.; Budimir, M.; Davis, M.; Setter, N. Piezoelectric Anisotropy: Enhanced Piezoelectric Response along Nonpolar Directions in Perovskite Crystals. *J. Mater. Sci.* **2006**, *41*, 65−76.

(6) Callori, S. J.; Gabel, J.; Su, D.; Sinsheimer, J.; Fernandez-Serra, M. V.; Dawber, M. Ferroelectric $PbTiO_3/SrRuO_3$ Superlattices with Broken Inversion Symmetry. *Phys. Rev. Lett.* **2012**, *109*, 067601.

(7) Kentgens, A. P. M.; Carim, A. H.; Dam, B. Transmission Electron Microscopy of Thin $YBa_2Cu_3O_{[7-x]}$ Films on (001) $SrTiO_3$ Prepared by DC Triode Sputtering. *J. Cryst. Growth* **1988**, *91*, 355−362.

(8) Bhalla, A. S.; Guo, R.; Roy, R. The Perovskite Structure − A Review of Its Role in Ceramic Science and Technology. *Mater. Res. Innovations* **2000**, *4*, 3−26.

(9) Wolfram, T. and Ellialtioglu, S.. *Electronic and Optical Properties of D-Band Perovskites*. Cambridge University Press: Cambridge, 2006.

(10) Tokura, Y.; Nagaosa, N. Orbital Physics in Transition-Metal Oxides. *Science* **2000**, *288*, 462−468.

(11) McCormack, M.; Jin, S.; Tiefel, T. H.; Fleming, R. M.; Phillips, J. M.; Ramesh, R. Very Large Magnetoresistance in Perovskite-like La-Ca-Mn-O Thin Films. *Appl. Phys. Lett.* **1994**, *64*, 3045−3047.

(12) Reagor, D. W.; Butko, V. Y. Highly Conductive Nanolayers on Strontium Titanate Produced by Preferential Ion-Beam Etching. *Nat. Mater.* **2005**, *4*, 593−596.

(13) Xu, G.; Ren, Z.; Du, P.; Weng, W.; Shen, G.; Han, G. Polymer-Assisted Hydrothermal Synthesis of Single-Crystalline Tetragonal Perovskite $PbZr_{[0.52]}Ti_{[0.48]}O_3$ Nanowires. *Adv. Mater.* **2005**, *17*, 907−910.

(14) Joshi, U. A.; Lee, J. S. Template-Free Hydrothermal Synthesis of Single-Crystalline Barium Titanate and Strontium Titanate Nanowires. *Small* **2005**, *1*, 1172−1176.

(15) Vasseur, S.; Duguet, E.; Portier, J.; Goglio, G.; Mornet, S.; Hadová, E.; Knížek, K.; Maryško, M.; Veverka, P.; Pollert, E. Lanthanum Manganese Perovskite Nanoparticles as Possible in Vivo Mediators for Magnetic Hyperthermia. *J. Magn. Magn. Mater.* **2006**, *302*, 315−320.

(16) Mao, Y.; Wong, S. S. Composition and Shape Control of Crystalline $Ca_{[1-x]}Sr_{[x]}TiO_3$ Perovskite Nanoparticles. *Adv. Mater.* **2005**, *17*, 2194−2199.

(17) Goncalves-Ferreira, L.; Redfern, S. A. T.; Artacho, E.; Salje, E. K. H. Ferrielectric Twin Walls in $CaTiO_3$. *Phys. Rev. Lett.* **2008**, *101*, 097602.

(18) Van Aert, S.; Turner, S.; Delville, R.; Schryvers, D.; Van Tendeloo, G.; Salje, E. K. H Direct Observation of Ferrielectricity at Ferroelastic Domain Boundaries in $CaTiO_3$ by Electron Microscopy. *Adv. Mater.* **2012**, *24*, 523−527.

(19) Vlahos, E.; Lummen, T.; Haislmaier, R.; Denev, S.; Brooks, C.; Biegalski, M.; Schlom, D. Ferroelectricity in $CaTiO_3$ Single Crystal Surfaces and Thin Films and Probed by Nonlinear Optics and Raman Spectroscopy. *APS Meeting Abstracts* **2011**, 22004 http://adsabs.harvard.edu/abs/2011APS..MARY22004V.

(20) Krause, A.; Weber, W. M.; Schröder, U.; Pohl, D.; Rellinghaus, B.; Heitmann, J.; Mikolajick, T. Reduction of Leakage Currents with Nanocrystals Embedded in an Amorphous Matrix in Metal-Insulator-Metal Capacitor Stacks. *Appl. Phys. Lett.* **2011**, *99*, 222905−222905-3.

(21) Abe, K.; Komatsu, S. Epitaxial Growth of $SrTiO_3$ Films on Pt Electrodes and Their Electrical Properties. *Jpn. J. Appl. Phys., Part 1* **1992**, *31*, 2985−2988.

(22) Son, J.; Cagnon, J.; Boesch, D. S.; Stemmer, S. Epitaxial $SrTiO_3$ Tunnel Barriers on Pt/MgO Substrates. *Appl. Phys. Express* **2008**, *1*, 061603.

(23) Adachi, M., Akishige, Y.; Asahi, T.; Deguchi, K.; Gesi, K.; Hasebe, K.; Hikita, T., et al. $CaTiO_3$, 1A-7. In *Numerical Data and Functional Relationships in Science and Technology. Group III Condensed Matter*. Vol. *36A1*: Oxides, Springer: Berlin, 2002; pp 1−18. http://dx.doi.org/10.1007/10426842_32.

(24) Lee, J.-S.; Joo, S.-K. The Problems Originating from the Grain Boundaries in Dielectric Storage Capacitors. *Solid-State Electron.* **2002**, *46*, 1651−1657.

(25) McKenna, K.; Shluger, A.; Iglesias, V.; Porti, M.; Nafría, M.; Lanza, M.; Bersuker, G. Grain Boundary Mediated Leakage Current in Polycrystalline HfO_2 Films. *Microelectron. Eng.* **2011**, *88*, 1272−1275.

(26) Jeon, W.; Chung, H.-S.; Joo, D.; Kang, S.-W. $TiO_2/Al_2O_3/TiO_2$ Nanolaminated Thin Films for DRAM Capacitor Deposited by Plasma-Enhanced Atomic Layer Deposition. *Electrochem. Solid-State Lett.* **2008**, *11*, H19−H21.

(27) Krause, A.; Weber, W.; Jahn, A.; Richter, K.; Pohl, D.; Rellinghaus, B.; Schroder, U.; Heitmann, J.; Mikolajick, T. Evaluation of the Electrical and Physical Properties of Thin Calcium Titanate High-K Insulators for Capacitor Applications. *J. Vac. Sci. Technol. B* **2011**, *29*, 01AC07.

(28) Weinreich, W.; Wilde, L.; Müller, J.; Sundqvist, J.; Erben, E.; Heitmann, J.; Lemberger, M.; Bauer, A. J. Structural Properties of As Deposited and Annealed ZrO_2 Influenced by Atomic Layer Deposition, Substrate, and Doping. *J. Vac. Sci. Technol. A* **2013**, *31*, 01A119.

(29) Aarik, J.; Aidla, A.; Mändar, H.; Uustare, T.; Sammelselg, V. Growth Kinetics and Structure Formation of ZrO_2 Thin Films in Chloride-Based Atomic Layer Deposition Process. *Thin Solid Films* **2002**, *408*, 97−103.

(30) Zacharias, M.; Bläsing, J.; Veit, P.; Tsybeskov, L.; Hirschman, K.; Fauchet, P. M. Thermal Crystallization of Amorphous Si/SiO_2 Superlattices. *Appl. Phys. Lett.* **1999**, *74*, 2614.

(31) Wei, X.; Luping, S.; Chong, C. T.; Rong, Z.; Koon, L. H. Thickness Dependent Nano-Crystallization in $Ge_2Sb_2Te_5$ Films and Its Effect on Devices. *Jpn. J. Appl. Phys.* **2007**, *46*, 2211−2214.

(32) AMCSD Database entry #0011157 for fcc Pt ($Fm3m$).

(33) Yamanaka, T.; Hirai, N.; Komatsu, Y. Structure Change of $Ca_{[1-x]}Sr_{[x]}TiO_3$ Perovskite with Composition and Pressure. *Am. Mineral.* **2002**, *87*, 1183−1189.

(34) Asthagiri, A.; Niederberger, C.; Francis, A. J.; Porter, L. M.; Salvador, P. A.; Sholl, D. S. Thin Pt Films on the Polar $SrTiO_3$ (111) Surface: An Experimental and Theoretical Study. *Surf. Sci.* **2003**, *537*, 134−152.

(35) Asthagiri, A.; Sholl, D. S. DFT Study of Pt Adsorption on Low Index $SrTiO_3$ Surfaces: $SrTiO_3$ (100), $SrTiO_3$ (111) and $SrTiO_3$ (110). *Surf. Sci.* **2005**, *581*, 66−87.

(36) Muralt, P.; Maeder, T.; Sagalowicz, L.; Hiboux, S.; Scalese, S.; Naumovic, D.; Agostino, R. G.; et al. Texture Control of $PbTiO_3$ and $Pb(Zr,Ti)O_3$ Thin Films with TiO_2 Seeding. *J. Appl. Phys.* **1998**, *83*, 3835−3841.

(37) Lüth, H.. *Solid Surfaces, Interfaces and Thin Films*. Springer-Verlag: New York, 2010.

(38) Ohring, M. Thin-Film Evaporation Processes. In *Materials Science of Thin Films*, 2nd ed.; Academic Press: Boston, 2002; Chapter 3, pp 95−144. http://www.sciencedirect.com/science/article/pii/B9780125249751500069

(39) Albe, K.; Nordlund, K.; Averback, R. S. Modeling the Metal-Semiconductor Interaction: Analytical Bond-Order Potential for Platinum−Carbon. *Phys. Rev. B: Condens. Matter Mater. Phys.* **2002**, *65*, 195124.

(40) Dannenberg, A.; Gruner, M. E.; Hucht, A.; Entel, P. Surface Energies of Stoichiometric FePt and CoPt Alloys and Their Implications for Nanoparticle Morphologies. *Phys. Rev. B: Condens. Matter Mater. Phys.* **2009**, *80*, 245438.

(41) Lyon, H. B.; Somorjai, G. A. Low-Energy Electron-Diffraction Study of the Clean (100), (111), and (110) Faces of Platinum. *J. Chem. Phys.* **1967**, *46*, 2539−2550.

(42) Harp, G. R.; Farrow, R. F. C.; Marks, R. F.; Vazquez, J. E. Epitaxial Growth and Homoepitaxy of Pt (110) and Cu (110) on $SrTiO_3$ (110). *J. Cryst. Growth* **1993**, *127*, 627−633.

(43) Eglitis, R. I.; Vanderbilt, D. Ab Initio Calculations of the Atomic and Electronic Structure of $CaTiO_3$ (001) and (011) Surfaces. *Phys. Rev. B: Condens. Matter Mater. Phys.* **2008**, *78*, 155420.

(44) Eglitis, R. I. First-Principles Calculations of the Atomic and Electronic Structure of $CaTiO_3$ (111) Surfaces. *Ferroelectrics* **2011**, *424*, 1−6.

(45) Zhang, J.-M.; Cui, J.; Xu, K.-W.; Ji, V.; Man, Z.-Y. Ab Initio Modeling of $CaTiO_3$ (110) Polar Surfaces. *Phys. Rev. B: Condens. Matter Mater. Phys.* **2007**, *76*, 115426.

(46) Wang, Y. X.; Arai, M.; Sasaki, T.; Wang, C. L. First-Principles Study of the (001) Surface of Cubic $CaTiO_3$. *Phys. Rev. B: Condens. Matter Mater. Phys.* **2006**, *73*, 035411.

(47) Liu, W.; Wang, C.; Cui, J.; Man, Z.-Y. Ab Initio Calculations of the $CaTiO_3$ (111) Polar Surfaces. *Solid State Commun.* **2009**, *149*, 1871−1876.

(48) Eglitis, R. I.; Rohlfing, M. First-Principles Calculations of the Atomic and Electronic Structure of $SrZrO_3$ and $PbZrO_3$ (001) and (011) Surfaces. *J. Phys.: Condens. Matter* **2010**, *22*, 415901.

(49) Schmidt, V.; Senz, S.; Gösele, U. Diameter-Dependent Growth Direction of Epitaxial Silicon Nanowires. *Nano Lett.* **2005**, *5*, 931−935.

(50) Dawber, M.; Szafraniak, I.; Alexe, M.; Scott, J. F. Self-Patterning of Arrays of Ferroelectric Capacitors: Description by Theory of Substrate Mediated Strain Interactions. *J. Phys.: Condens. Matter* **2003**, *15*, L667.

(51) Vasco, E.; Dittmann, R.; Karthäuser, S.; Waser, R. Early Self-Assembled Stages in Epitaxial $SrRuO_3$ on $LaAlO_3$. *Appl. Phys. Lett.* **2003**, *82*, 2497−99.

(52) Muralt, P. Texture Control and Seeded Nucleation of Nanosize Structures of Ferroelectric Thin Films. *J. Appl. Phys.* **2006**, *100*, 051605.

(53) Martin, D.; Grube, M.; Weber, Walter M.; Rüstig, J.; Bierwagen, O.; Geelhaar, L.; Riechert, H. Local Charge Transport in Nanoscale Amorphous and Crystalline Regions of High-K $(ZrO_2)_{[0.8]}(Al_2O_3)_{[0.2]}$ Thin Films. *Appl. Phys. Lett.* **2009**, *95*, 142906.

(54) Bierwagen, O.; Geelhaar, L.; Gay, X.; Piešiņš, M.; Riechert, H.; Jobst, B.; Rucki, A. Leakage Currents at Crystallites in $ZrAl_{[x]}O_{[y]}$ Thin Films Measured by Conductive Atomic-Force Microscopy. *Appl. Phys. Lett.* **2007**, *90*, 232901.

(55) Heitmann, J.; Müller, F.; Zacharias, M.; Gösele, U. Silicon Nanocrystals: Size Matters. *Adv. Mater.* **2005**, *17*, 795−803.

(56) Zacharias, M.; Streitenberger, P. Crystallization of Amorphous Superlattices in the Limit of Ultrathin Films with Oxide Interfaces. *Phys. Rev. B: Condens. Matter Mater. Phys.* **2000**, *62*, 8391.

(57) Spinella, C.; Lombardo, S.; Priolo, F. Crystal Grain Nucleation in Amorphous Silicon. *J. Appl. Phys.* **1998**, *84*, 5383−5414.